Earth and Planetary Science Letters 544 (2020) 116383

Contents lists available at ScienceDirect

Earth and Planetary Science Letters

www.elsevier.com/locate/epsl

Late Pliocene onset of the Cona rift, eastern Himalaya, confirms eastward propagation of extension in Himalayan-Tibetan orogen

Shuang Bian[a,b], Junfeng Gong[a,b,*], Andrew V. Zuza[c], Rong Yang[a,b], Yuntao Tian[d], Jianqing Ji[e], Hanlin Chen[a,b], Qinqin Xu[f], Lin Chen[g], Xiubin Lin[a,b], Xiaogan Cheng[a,b], Jiyao Tu[e], Xiangjiang Yu[h]

[a] *Key Laboratory of Geoscience Big Data and Deep Resource of Zhejiang Province, School of Earth Sciences, Zhejiang University, Hangzhou 310027, China*
[b] *Research Center for Structures in Oil and Gas Bearing Basins, Ministry of Education, Hangzhou 310027, China*
[c] *Nevada Bureau of Mines and Geology, University of Nevada, Reno, NV 89557, USA*
[d] *School of Earth Sciences and Engineering, Sun Yat-sen University, Guangzhou 510275, China*
[e] *School of Earth and Space Sciences, Peking University, Beijing 100871, China*
[f] *Institute of Geology, Chinese Academy of Geological Sciences, Beijing 100037, China*
[g] *Institute of Geology and Geophysics, Chinese Academy of Sciences, Beijing 100029, China*
[h] *College of Earth Sciences, Jilin University, Changchun 130061, China*

ARTICLE INFO

Article history:
Received 10 December 2019
Received in revised form 28 May 2020
Accepted 30 May 2020
Available online xxxx
Editor: R. Bendick

Keywords:
Himalaya
Cona rift
east-west extension
low-temperature thermochronology
eastward younging rifting

ABSTRACT

Several competing hypotheses have been proposed to explain east-west extension observed across the Himalayan orogen, based primarily on observations from the western and central Himalaya. They make predictions for the temporal and spatial patterns of deformation in the eastern Himalaya. These tectonic models include radial spreading or oroclinal bending of the Himalayan arc, oblique convergence of the Indian continent, tearing or lateral detachment of the Indian slab and eastward flow of lithosphere. Here, for the first time we constrain the activity history of the Cona rift, the only north-trending rift currently recognized in the eastern Himalaya, based on biotite and K-feldspar ^{40}Ar/^{39}Ar and zircon and apatite (U–Th)/He thermochronology, to evaluate these proposed rifting mechanisms. Low-temperature thermochronological results suggest that the Cona rift is the youngest rift system in the Himalayas: after a slow phase of exhumation since ∼14 Ma (∼0.2–0.13 mm/yr), normal faulting initiated here at ∼3.0–2.3 Ma with a fault slip rate of ∼3.8–1.6 mm/yr and a horizontal extension magnitude of ∼2–5 km. Analysis of rifting across the Himalayas shows that rift initiation ages young eastward, which is matched by eastward decreasing rift-extension magnitudes. Monotonically eastward younging rift development is consistent with the tectonic model involving eastward lithospheric flow driven by Indian slab dynamics and coupled asynchronous gravitational potential energy gradients.

1. Introduction

The Himalayan orogen is the largest and youngest continent-continent collisional fold-thrust belt on Earth (Yin and Harrison, 2000) and is an archetypical example of an orogenic system undergoing active syncontractional extension accommodated by numerous parallel north-trending rifts (Fig. 1; e.g., Armijo et al., 1986). The even spacing between rifts implies a related geodynamic driving mechanism, and over the past several decades, numerous tectonic models have been proposed to explain east-west (E–W) extension in the Himalayas. Proposed hypotheses predict distinct patterns for the timing of rift initiation across the Himalayas (Supplementary Material Table S1). Convective thinning of lithospheric mantle (England and Houseman, 1989), a change in boundary conditions along Asia's eastern margin (Yin, 2010) and radial spreading (Seeber and Armbruster, 1984) models suggest nearly coeval initiation of these rifts. Dissimilarly, oroclinal bending of the Himalayan arc (Klootwijk et al., 1985), oblique convergence of the Indian plate (McCaffrey and Nabelek, 1998) and lateral slab detachment (Webb et al., 2017) models presume earlier initiation of the rifts close to the two ends of the Himalayan arc than those in the center (or center-east). Alternatively, grav-

---

[*] Corresponding author at: Key Laboratory of Geoscience Big Data and Deep Resource of Zhejiang Province, School of Earth Sciences, Zhejiang University, Hangzhou 310027, China.

E-mail address: jfgong@zju.edu.cn (J. Gong).

https://doi.org/10.1016/j.epsl.2020.116383

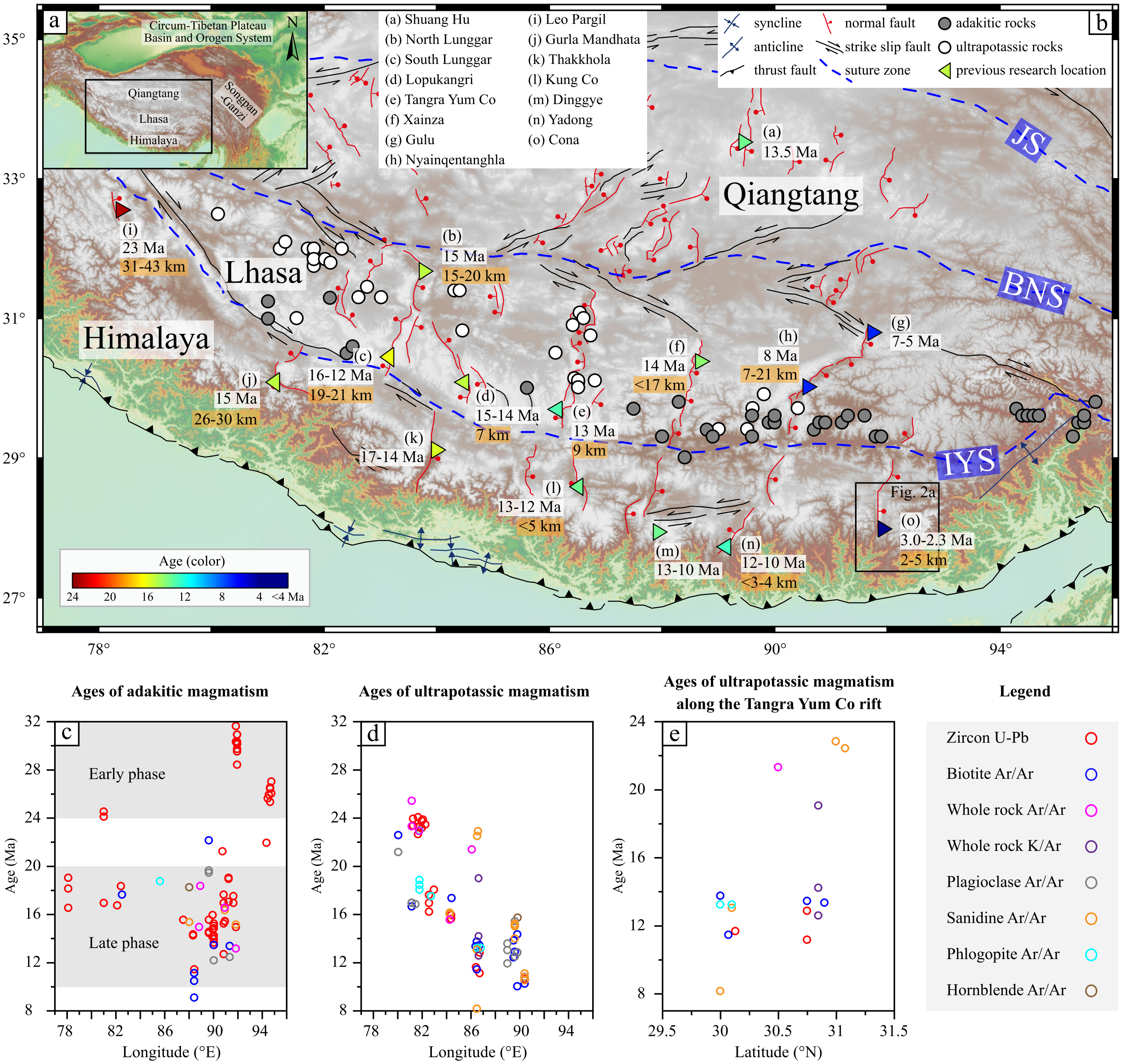

Fig. 1. (a) Sketch of the Himalayan-Tibetan system and surrounding areas. (b) Tectonic map of the Himalayas and the southern Tibet with major structures. Triangles denote the locations of previous research for normal faults, the orientation and color of which represent the dip of the normal faults bounding the rifts and the initiation time, respectively. The black and white circles denote the locations for adakitic and ultrapotassic rocks in the Lhasa terrane, respectively. Detailed descriptions can be found in the Supplementary Material and Tables S2, S3, S4. Key to symbols: BNS: Bangong Nujiang suture; IYS: Indus-Yarlung suture; JS: Jinsha suture. (c) Longitudinal variations in ages of adakitic magmatism without uncertainties. They show two phases of activities with the early phase of >24 Ma not displaying any clear trend, whereas the later phase of <20 Ma representing an eastward younging trend. (d) Longitudinal variations in ages of ultrapotassic magmatism without uncertainties. They display an eastward younging trend. (e) Ages of ultrapotassic magmatism along the Tangra Yum Co rift without uncertainties. They display a southward younging trend. (For interpretation of the colors in the figure(s), the reader is referred to the web version of this article.)

itational collapse-driven eastward flow of lithosphere (Yin and Taylor, 2011; Bischoff and Flesch, 2018) model predicts extension to follow the development of excess gravitational potential energy (GPE). If GPE developed asynchronously and was greater in the west than the east, due in part to a narrower Himalayan-Tibetan orogen in the west (e.g., Yang and Liu, 2013) and/or Greater Indian collisional geometry (e.g., Meng et al., 2020), these models predict a broad eastward younging Himalayan rifting. Therefore, constraining the spatiotemporal pattern of rifting is a critical test of these proposed hypotheses.

Modern geochronological studies of the initiation ages of rifting are mainly concentrated in the western and central Himalaya, which shows an eastward younging trend (Fig. 1b; Table. S2). That is, extension youngs from the ~23 Ma Leo Pargil rift at the west (Langille et al., 2012) to the ~12–10 Ma Yadong rift at the center-east (Edwards and Harrison, 1997; Xu et al., 2013). To evaluate the complete pattern of Himalayan rifting and compare with the above model predictions, the timing of extensional deformation in the eastern Himalaya is required. The initiation history of the Cona rift, the only rift system currently recognized in the east-

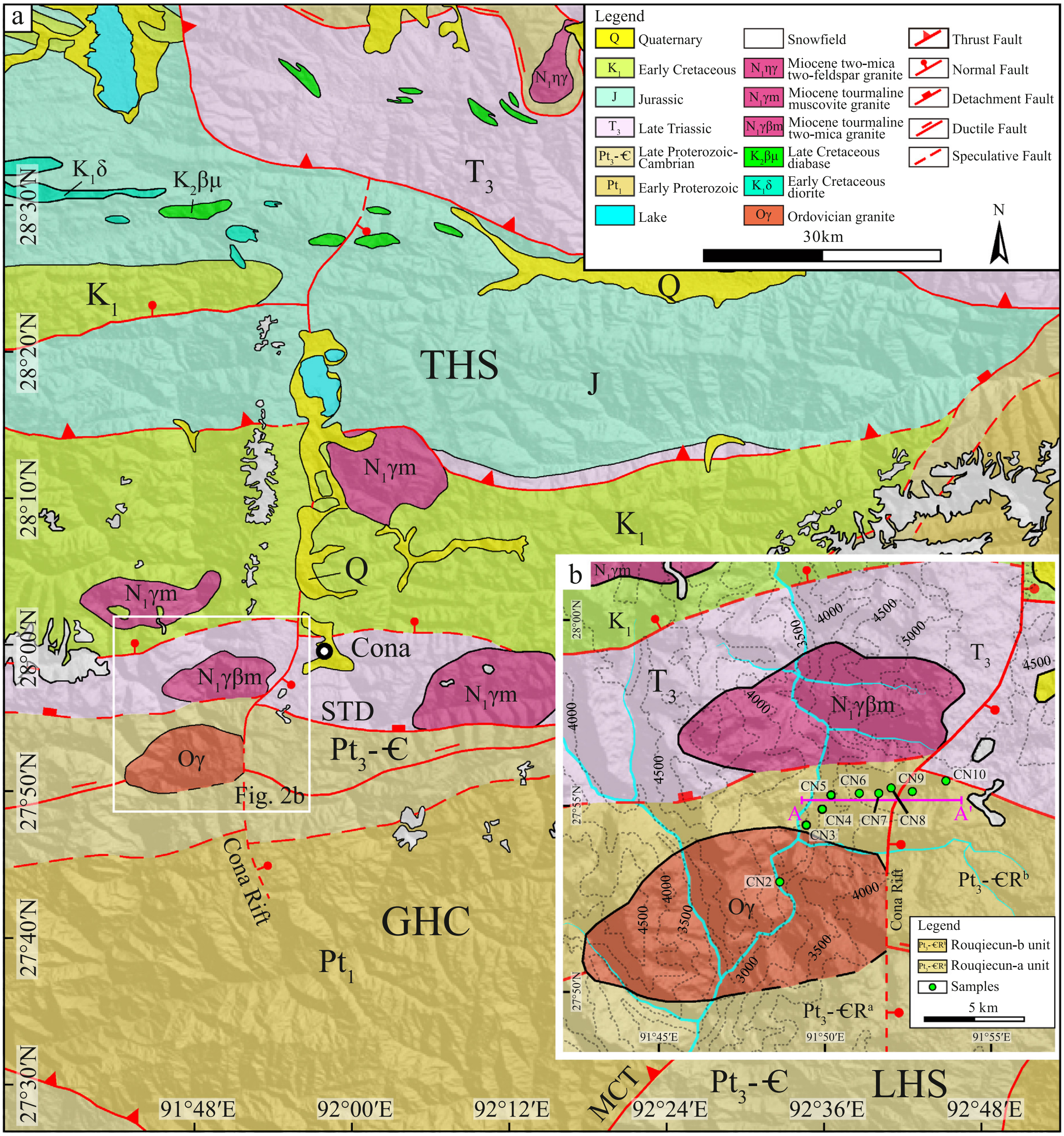

Fig. 2. (a) Regional geologic map of the Cona area modified after Bureau of Yunnan Geological Survey (2004). (b) Sampling sites from this study of the Cona rift. Green circles show samples collected for thermochronological analysis. Key to symbols: STD: South Tibet Detachment; MCT: Main Central Thrust; LHS: Lesser Himalayan Sequence; GHC: Greater Himalayan Crystalline Complex; THS: Tethyan Himalayan Sequence.

ern Himalaya (Fig. 1b), remains entirely unconstrained. Without thermochronological data from the Cona rift, two Himalayan rift-initiation patterns are possible based on published data from the other rifts (Fig. 1b). One is a bidirectional younging trend toward the central-east Himalaya when the Cona rift initiated earlier than the Yadong rift at the west, and the other one is a monotonic eastward younging trend if the Cona rift initiated more recently. In this regard, the Cona rift offers an excellent opportunity to better constrain the Himalayan rifting process and to evaluate current tectonic models.

In this study, we report new biotite and K-feldspar $^{40}Ar/^{39}Ar$ and zircon and apatite (U–Th)/He thermochronological data for samples collected along the southern segment of the Cona rift (Fig. 2). By constraining the initiation age of the Cona fault, we provide new insights on the mechanism of E–W extension in the Himalayan-Tibetan orogen.

2. Geologic setting

2.1. E–W extension in the eastern Himalaya and Cona region geology

The interior of the Himalayan-Tibetan system comprises five units, which from south to north are the Himalaya, and the Lhasa, Qiangtang, Songpan-Ganzi, and Qaidam-Qilian terranes separated by the Indus-Yarlung, Bangong-Nujiang, Jinsha, and Anyimaqen-Kunlun-Muztagh suture zones, respectively (Fig. 1a; Yin and Harrison, 2000; Zuza et al., 2018). Both the Himalayan orogen and southern Tibet (i.e., regions south of the Jinsha suture zone) are characterized by widespread E–W extension accommodated by a series of north-trending rifts and conjugate strike-slip faults along the Bangong-Nujiang suture (BNS) (Fig. 1b; Armijo et al., 1986; Taylor et al., 2003; Yin and Taylor, 2011). Herein, we refer to the eastern Himalaya as the region east of the Yadong rift, where there

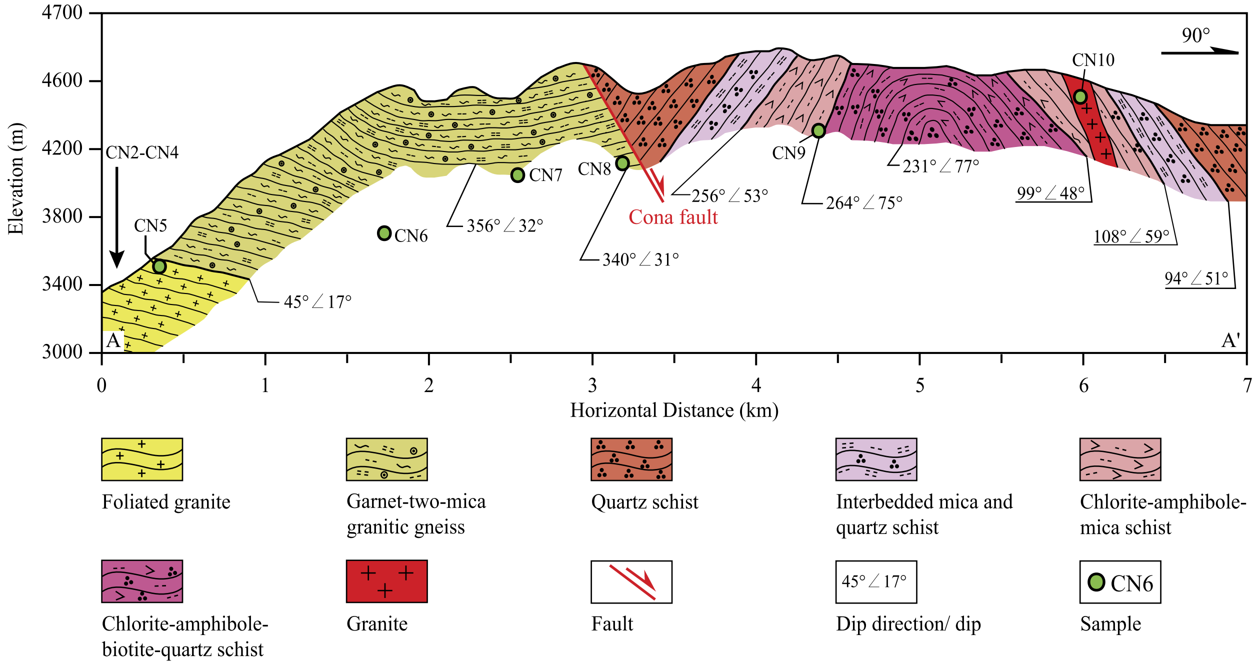

Fig. 3. True-scale cross section of the Cona fault (A-A′ on Fig. 2b) with sampling locations.

are changes in GPS velocity field, from NNE-directed rotating clockwise to NE-directed (Zheng et al., 2017), and in Himalayan arc curvature (Bendick and Bilham, 2001; Webb et al., 2017). To the west of the Yadong rift, the region is the western and central Himalaya separated by the Gurla Mandhata rift.

In the eastern Himalaya, E–W extension is accommodated by the ∼150-km-long north-trending Cona rift, a half graben bounded by the east-dipping Cona normal fault at the west. It is the southern part of the Woka-Cona rift zone and is connected to the west-dipping Woka normal fault to the north of the Indus-Yarlung suture (IYS) (Fig. 1b; Yin et al., 2010). The whole rift zone stretches from the Lhasa terrane in the north southward into the Lesser Himalayan Sequence (LHS) (Figs. 1b, 2a), offsetting major structures such as the IYS, Great Counter Thrust, North Himalayan Antiform, Tethyan Himalayan fold-thrust belt, and South Tibet Detachment (STD) (Yin et al., 2010; Webb et al., 2013). The southern segment of the Cona fault, on which this study focuses, strikes ∼190° and dips 60° east. It offsets the west-dipping rocks of the hanging wall against the north-dipping rocks of the footwall (Fig. 3), producing a topographic depression near the fault scarp. The hanging wall is mainly composed of various schist units including quartz schist, interbedded quartz schist and mica schist, chlorite-amphibole-mica schist and chlorite-amphibole-biotite-quartz schist, while the footwall mainly consists of foliated granite and garnet-bearing two-mica granitic gneiss.

Lithologies in the Cona region include the LHS, Greater Himalayan Crystalline Complex (GHC) and Tethyan Himalayan Sequence (THS) (Fig. 2a; Yin et al., 2010; Webb et al., 2013). The LHS consists of the Neoproterozoic-Cambrian strata that comprise clastic rocks, carbonate rocks, volcanic rocks, schist and phyllite. The GHC, overlying on the LHS bounded by the Main Central Thrust (MCT), consists of Paleoproterozoic metamorphic rocks that comprise various schists and gneisses and Neoproterozoic-Cambrian metamorphic rocks that comprise amphibolite, schist and phyllite. These rocks have undergone amphibolite and granulite facies metamorphism. The THS is unconformably seated on top of the GHC bounded by the STD. It consists of Mesozoic strata including Upper Triassic, Jurassic, Lower Cretaceous sedimentary rocks, all of which are faulted against its overlying strata. The strata in the Cona region were intruded by various episodes of plutons or dikes, such as Ordovician and Miocene granites, Cretaceous diabases (sillites) and diorites (Fig. 2; Bureau of Yunnan Geological Survey, 2004).

2.2. Post-collisional magmatism in southern Tibet

Post-collisional adakitic and ultrapotassic rocks are extensively exposed in the Lhasa terrane (Zhang et al., 2014; Guo and Wilson, 2019) and have widely been accepted to reflect post-collisional tectonic processes. Ultrapotassic rocks are thought to be derived from the partial melting of enriched lithospheric mantle (Xu et al., 2017; Wang et al., 2018), whereas the source of adakitic rocks can be ambiguous, resulting from melts of overthickened crust, upper mantle or oceanic/lithospheric crust (Zhang et al., 2014, and references therein). Tectonic models for the generation of both ultrapotassic and adakitic rocks include convective thinning of Asian lithospheric mantle (Turner et al., 1996), breakoff or detachment of Neo-Tethyan oceanic or Indian continental slab (Lu et al., 2019), intracontinental subduction (Tapponnier et al., 2001), and tearing of Indian continental slab (Hou et al., 2006). Despite debate about their exact generation mechanism, their existence is caused by a broadly similar tectonic process that involved asthenospheric upwelling due to slab deformation. This implies the important role played by the subducted Neo-Tethyan oceanic or Indian continental slabs, such as their subduction, rollback, detachment or tearing.

In southern Tibet, adakitic rocks are distributed within a narrow belt subparallel to the IYS (Fig. 1b) and show two phases of activities (Fig. 1c; Table S3; Lu et al., 2019) with the early phase of >24 Ma not displaying any clear trend, whereas the later phase of <20 Ma representing an eastward younging trend (Fig. 1c). The two phases of adakitic rocks are characterized by different fractionation evolutions of light and medium rare earth elements and proposed to be related to breakoff of the Neo-Tethyan oceanic and Indian continental slabs, respectively (Lu et al., 2019).

Exposures of ultrapotassic rocks follow two spatial trends, with most of them generally distributed along an east-trending belt across the Lhasa terrane that young eastward (Figs. 1b, d; Table S4). A lesser amount is exposed along the north-trending rifts, such as the Tangra Yum Co rift, and the ages young southward (Fig. 1e; Table S4; Guo and Wilson, 2019). These two distinct spatiotemporal patterns for the ultrapotassic rocks imply a compound process, rather than a single process (e.g., slab detachment or tearing), for their generation.

3. Sampling and analytical methods

3.1. Sampling

To constrain the exhumation history associated with the Cona rift, we performed $^{40}Ar/^{39}Ar$ and (U–Th)/He thermochronology. Nine samples (CN2 through CN10) were collected within a horizontal distance of ~8 km across the southern segment of the Cona rift (Fig. 2b). Samples CN2 through CN8 were from the footwall and CN9 and CN10 were from the hanging wall with sample elevations ranging >1.5 km from 2970 m (CN2) to 4526 m (CN10). Samples CN3 and CN10 were collected from granite, CN4 and CN5 from foliated granite, CN9 from mica-bearing schist, and CN2, CN6, CN7 and CN8 from granitic gneiss. All the nine samples provided adequate biotite grains for $^{40}Ar/^{39}Ar$ dating and only sample CN10 also provided suitable K-feldspar for $^{40}Ar/^{39}Ar$ dating. Seven samples (CN2, CN3, CN6, CN7, CN8, CN9 and CN10) provided enough apatite grains and two samples (CN2 and CN8) provided enough zircon grains for (U–Th)/He dating, respectively.

3.2. $^{40}Ar/^{39}Ar$ thermochronology

The $^{40}Ar/^{39}Ar$ measurements on both biotite and K-feldspar were conducted at the Key Laboratory of Orogenic Belt and Crustal Evolution, Peking University. Biotite and K-feldspar grains were separated by crushing, sieving, heavy liquid and magnetic separation. Separates were ultrasonically cleaned in deionized water and dried at ~100 °C. Subsequently, samples, standards and the crystals of K_2SO_4, CaF_2, KCl were weighed and packaged into aluminum foils. The packages were then sealed in a vacuum quartz bottle and irradiated at China Institute of Atomic Energy in Beijing. The samples were dated by the step-heating method to determine the age of the released argon gas at each temperature step. Finally, plateau ages and corresponding isochron ages were calculated using Isoplot 3.0 (Ludwig, 2003). Errors in the age calculations are presented as 2σ uncertainties. Age spectra and corresponding inverse isochron ages as well as analytical results are listed in the Supplementary Material (Fig. S1; Table S5).

3.3. (U–Th)/He thermochronology

The (U–Th)/He dating on both apatite and zircon was performed at the University of Melbourne and University College London, following standard procedures. Apatite and zircon grains were separated by heavy liquid and magnetic separation. At least three grains with euhedral morphology and no visible inclusions were then handpicked for each sample except sample CN9 where only two apatite grains were selected. To minimize alpha-ejection associated with ^4He diffusion, only grains with both length and width greater than 60 μm were selected. Samples were heated by a diode laser to release the stored ^4He and then were put into a quadrupole mass spectrometer for ^4He measurement. For degassing helium from zircons, a re-heating at a higher temperature was performed. After degassing, those grains were dissolved for measurement of U–Th concentrations by an inductively coupled plasma mass spectrometer (ICP-MS). The (U–Th)/He ages were calculated and corrected following the approach of Farley et al. (1996). In this study, we used the mean age of each sample with an uncertainty of 5–6% (1σ) due to the analytical uncertainty in U, Th and He measurement and grain size. The analytical results of apatite and zircon (U–Th)/He dating are reported in Tables S6 and S7.

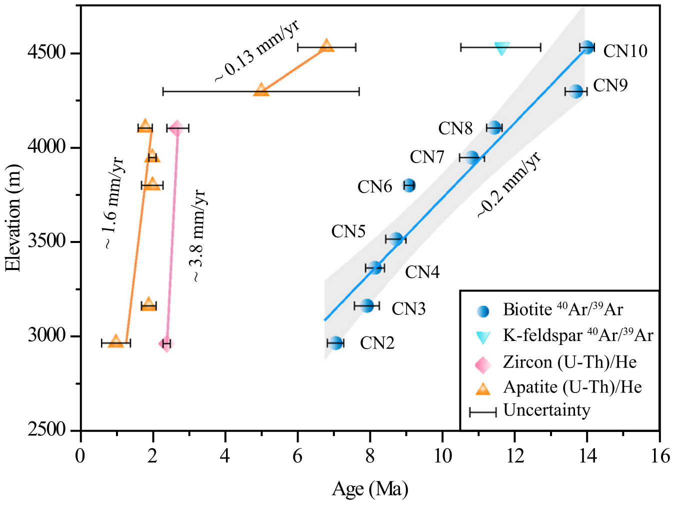

Fig. 4. Age-elevation diagram. The shaded region depicts 95% confidence intervals. Refer to the text for detailed explanations.

4. Results

Nine biotite samples yielded $^{40}Ar/^{39}Ar$ plateau ages ranging from 7.05 ± 0.22 to 13.97 ± 0.20 Ma. These ages are consistent with the inverse isochron ages of the same samples (Fig. S1), indicating no Ar excess or loss after the closure of minerals. Sample CN4 has a large uncertainty in its inverse isochron age. This is because the second to fifth heating steps have relatively large uncertainties, which is probably due to the heterogeneous distribution of Ar isotopes. However, we prefer that its plateau age is still reasonable as it is within the error range of inverse isochron containing reasonable age error (3%) and fits the general tendency of all the samples. Sample CN10 yielded a K-feldspar $^{40}Ar/^{39}Ar$ age of 11.52 ± 0.16 Ma and this age is younger than that of the biotite $^{40}Ar/^{39}Ar$ age (13.97 ± 0.20 Ma), which is consistent with the fact that the closure temperature of biotite (~350 °C) is higher than that of K-feldspar (~150–250 °C) (McDougall and Harrison, 1999).

The seven mean apatite (U–Th)/He ages vary from 1.0 ± 0.4 to 6.8 ± 0.8 Ma (Fig. 4; Table S6). The mean zircon (U–Th)/He ages of the three samples vary in a small range between 2.4 ± 0.1 and 2.7 ± 0.3 Ma (Fig. 4; Table S7). Each sample yielded replicable single-grain ages.

5. Discussion

5.1. Initiation time and extension magnitude of the Cona rift

To constrain the initiation time of Cona rift, we constructed age-elevation profiles from the $^{40}Ar/^{39}Ar$ and (U–Th)/He ages (Fig. 4). The biotite $^{40}Ar/^{39}Ar$ ages are positively correlated with the current elevations of the samples, demonstrating a moderately slow exhumation rate of ~0.2 mm/yr between ~14–7 Ma (Fig. 4). Although samples CN9 and CN10 were collected from the hanging wall, their ages do not deviate from the linear age-elevation relationship between all samples (Fig. 4). Thus, we argue that those biotite $^{40}Ar/^{39}Ar$ ages record regional erosion and exhumation rather than fault-associated exhumation. Such a slow exhumation rate of ~0.2 mm/yr matches data from Tremblay et al. (2015) near Lhasa, southern Tibet, suggesting a slow regional exhumation rate from ~12–11 Ma to the present in the southern Tibetan Plateau margin.

Conversely, the apatite (U–Th)/He ages suggest two distinct age trends for the hanging wall and footwall rocks (Fig. 4). Above the elevation of ∼4100 m, the two hanging wall samples (CN9 and CN10) define a gentle slope and thus a much lower exhumation rate of ∼0.13 mm/yr between ∼7–5 Ma, which is comparable with that derived from the biotite ^{40}Ar/^{39}Ar ages. Below ∼4100 m, all the ages from the footwall of the fault show a steep slope, indicating an exhumation rate of ∼1.6 mm/yr between ∼2–1 Ma. We suggest that the much faster exhumation rate in the footwall (∼1.6 mm/yr) compared with the hanging wall (∼0.13 mm/yr) is related to initiation of the Cona normal fault system at, or just prior to, ∼2 Ma. Furthermore, this high exhumation rate in the footwall is additionally constrained by zircon (U–Th)/He results where ages are very close (2.7–2.4 Ma) with an elevation range of >1 km (4103 to 2970 m), suggesting a rapid exhumation rate of up to ∼3.8 mm/yr.

In summary, we infer that both sides of the Cona fault have experienced regional exhumation at a rate of ∼0.2 mm/yr since ∼14 Ma until ∼2.7 Ma when exhumation accelerated locally in the footwall at a rate of ∼3.8 mm/yr due to the initiation of the Cona normal fault (Fig. 4). Subsequently, fault activity slowed down to ∼1.6 mm/yr since ∼2.4 Ma. Using these exhumation rates, we integrate the total magnitude of exhumation at ∼7 km in the footwall of the Cona fault. Although the exhumation history is clearly constrained by our low-temperature thermochronological data, we still prefer to provide a conservative estimate for the timing of fault initiation into a range at 3.0–2.3 Ma, considering rapid exhumation along the whole profile of the footwall revealed by zircon (U–Th)/He data and uncertainties (Table S7).

Our interpreted fault-related exhumation accounts for ∼5 km in the footwall based on the estimated exhumation rates derived from (U–Th)/He data integrated over the timing of fault activity (Fig. 4), which overlaps the results deduced from cooling history of zircon (U–Th)/He system. Assuming a zircon (U–Th)/He closure temperature of 170–190 °C (Reiners et al., 2004), ∼4–8 km of vertical exhumation is implied using a geothermal gradient of ∼23–40 °C/km (Francheteau et al., 1984). The result corresponds to a horizontal extension magnitude of ∼2–5 km based on the 60° dip of the fault, implying a mean extension rate of ∼0.7–2.2 mm/yr. Relatively low offset magnitudes inferred from our thermochronological data are consistent with the small fault offsets along the Cona normal fault on the geologic map (Fig. 2). Additionally, the estimate is close to the ∼1.3–2.6 mm/yr extension rate in the Cona region by geodetic observation, which is calculated from the GPS velocity field based upon the difference in arc-parallel velocity component between the Cona and Yadong rifts (dataset from Zheng et al., 2017).

5.2. Spatiotemporal pattern of north-trending rifts in the Himalayas

The initiation ages for the north-trending rifts in the western and central Himalaya young eastward. In the Leo Pargil detachment zone (i in Fig. 1b), ductile shearing started at 23 Ma (Langille et al., 2012), which is interpreted as the initiation of rifting. To the east, extension in the Gurla Mandhata detachment fault zone (j in Fig. 1b) may have started as early as ∼15 Ma based on Pb-Th monazite dating of deformed and undeformed leucogranites (Murphy and Copeland, 2005). In the Thakkhola graben (k in Fig. 1b), extension began at ∼17 or 14 Ma as constrained by muscovite ^{40}Ar/^{39}Ar geochronology from north-trending hydrothermal veins (Coleman and Hodges, 1995) or from syn-extensional fabrics (Larson et al., 2020), respectively. Further east, in the Kung Co rift (l in Fig. 1b), the onset of normal faulting was constrained at 13–12 Ma by inverse modeling of zircon and apatite (U–Th)/He data (Lee et al., 2011), although this age was debated. The Dinggye rift (m in Fig. 1b) initiated at ∼13–10 Ma based on mica ^{40}Ar/^{39}Ar thermochronology (Kali et al., 2010), and the Yadong rift to the east (n in Fig. 1b) was proposed to be initiated after the cessation of motion along the STD (<10 Ma or ∼12 Ma; Edwards and Harrison, 1997; Xu et al., 2013). In summary, the above studies indicate that extension of the rifts propagated monotonically from the western Himalaya to the central Himalaya.

Our results demonstrate that the Cona normal fault initiated in the late Pliocene, which is significantly younger than all the other Himalayan rifts to the west (Fig. 1b; Table S2). This study extends the previously observed temporal pattern of rifting into the eastern Himalaya, suggesting a monotonic younging trend of rift initiation from the western Himalaya to the east. Similar to the trend of the initiation time of rifting, the horizontal extension component determined by both the slip magnitude along the rift and the dip angle of the fault (Table S8) also decreases eastward (Fig. 1b).

5.3. Working hypothesis for E–W extension in the Himalayas

The newly revealed monotonic eastward younging trend of rifting across the entire Himalaya provides crucial constraints to evaluate the mechanisms for E–W extension. This spatiotemporal pattern argues against several proposed hypotheses, such as those predicting regional coeval onset as in the convective thinning of lithospheric mantle, radial spreading, and gravitational collapse (assuming uniform topographic rise) models, or those implying a bidirectional center-ward younging trend as in the oroclinal bending, lateral slab detachment and oblique convergence models. A full description of all models can be found in the Supplementary Material. Here, we propose an integrated working hypothesis for E–W extension based on the spatiotemporal pattern of the north-treading rifts, two-phase adakitic magmatism (>24 Ma and 20–10 Ma), and the complex pattern of ultrapotassic magmatism (Fig. 1).

The Neo-Tethyan oceanic lithosphere broke off between ∼50 Ma and ∼40 Ma, which induced the asthenospheric upwelling and anatexis of the Lhasa terrane, generating the early phase of adakitic rocks (Fig. 5a; Lu et al., 2019). Subsequently, the Indian continental lithosphere continued to subduct, and started to detach laterally from the west since ∼25 Ma. This induced the progressive eastward emplacement of both the later phase of adakitic rocks (∼20–10 Ma) and the ultrapotassic rocks distributed along the east-trending belt at ∼25–8 Ma (Fig. 5b). When the Indian continental slab started detaching laterally, the remainder was released from the slab pull force, giving rise to its vertical motion. This caused topographic rise that built up local GPE in western Tibet above the slab segment released by detachment (Fig. 5b; Wortel and Spakman, 2000). As the slab detachment propagated eastward, the topographic rise migrated to follow slab detachment, leading to an asynchronous GPE gradient. This west-to-east migration of GPE was enhanced by the potentially narrower western Himalayan-Tibetan orogen that led to a higher strain rate and thus more rapid uplift in the west than in the east (Yang and Liu, 2013). Recent paleomagnetic observations suggest the geometry of the pre-collisional Greater India (Meng et al., 2020) may have resulted in earlier collision and more continental convergence in the west, thus leading to faster GPE buildup in the west than east. Later on, the GPE gradients drove eastward flow of lithosphere, inducing the development of north-trending rifts and associated v-shaped conjugate strike-slip faults along the BNS (Fig. 5b; Yin and Taylor, 2011; Zhang et al., 2013; Bischoff and Flesch, 2018).

Lithospheric flow may be accommodated by the whole lithosphere (Yin and Taylor, 2011) or only the lower crust (Bischoff and Flesch, 2018). Large scale low-velocity zone and anisotropy observed beneath Tibet (Yang et al., 2012; Zhang et al., 2013; Agius and Lebedev, 2017) and numerical modeling (Bischoff and Flesch, 2018) support eastward lower crustal flow, which may have been coupled with entire eastward lithospheric flow (Bendick and Flesch, 2007).

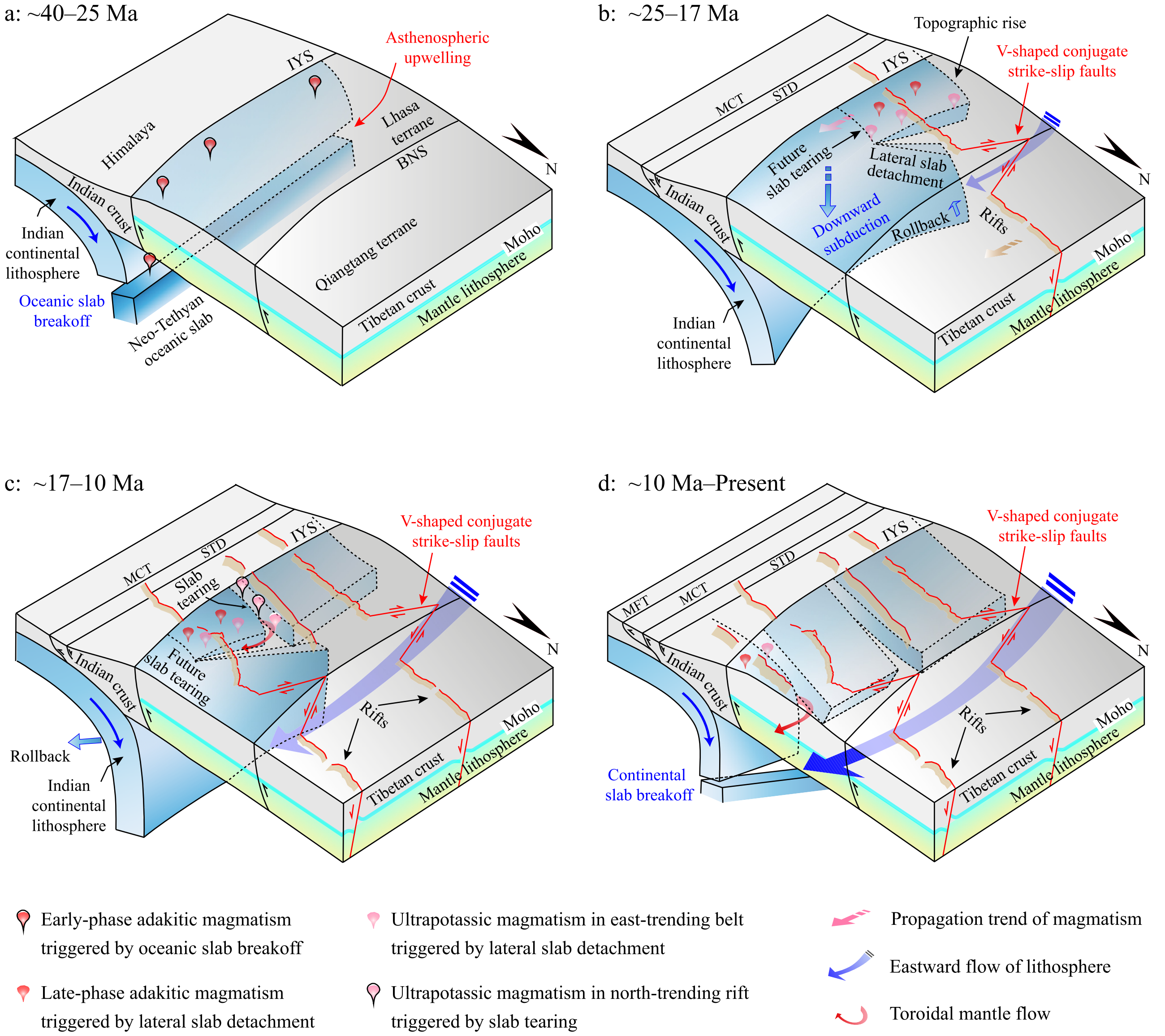

Fig. 5. Schematic diagrams of geodynamic processes for E–W extension in the Himalayan-Tibetan orogen. (a) ~40–25 Ma: the northward subducting of Neo-Tethyan oceanic lithosphere experienced slab breakoff, generating the early phase of adakitic magmatism. (b) ~25–17 Ma: as subduction continued, Indian lithospheric slab started to detach laterally from the west, generating the later phase of adakitic rocks and ultrapotassic rocks distributed in the east-trending belt; consequent local topographic rise driven by lateral slab detachment at western Tibet induced eastward flow of lithosphere, causing the v-shaped conjugate strike-slip faults and associated normal faults at its northern and southern ends. (c) ~17–10 Ma: progressive development of lateral slab detachment caused eastward-propagated dynamic topographic rise and resulted sequential north-trending rifting. Additionally, it also resulted in longitudinal slab tearing, giving rise to toroidal mantle flow around the slab edge and the southward generation of ultrapotassic rocks along the north-trending rifts. (d) ~10 Ma–Present: continuous slab deformation, dynamic topographic rise, and eastward lithospheric flow caused progressive development of a series of conjugate strike-slip faults and normal faults.

During the propagation of the lateral slab detachment, the subducting Indian lithosphere would have progressed differently along strike. In the west, the remainder of the lithosphere released by slab detachment would change its movement direction, from downward subduction to upward uplift. In the center-east, the slab remained coherent and would maintain its downward subduction into the mantle pulled by the attached slab (Fig. 5b). This kinematic difference between the detached and coherent segments could increase shear stress at their connection point. When accumulated stress at the connection point was beyond the ultimate strength of the Indian plate, the slab would break through to generate southward tearing (Figs. 5c, d). The resulting north-south tearing would generate a clockwise toroidal mantle flow around the broken slab edge (Figs. 5c, d; e.g., Zandt and Humphreys, 2008), which further enhanced eastward mantle flow parallel to the lateral slab detachment, contributing to the eastward propagation of E–W extension. At the same time, asthenospheric upwelling along the slab tearing triggered progressive southward production of ultrapotassic magmatic rocks in the southern Lhasa terrane distributed along the north-trending rifts (Fig. 5c; Guo et al., 2018; Guo and Wilson, 2019). This process may correspond with the low-velocity anomaly observed near the Tangra Yum Co rift (Liang et al., 2016).

The lateral detachment and tearing processes generated eastward migrating slab rollback relative to the Himalayas (Figs. 5b, c, d), giving rise to two effects. First, the rollback adjusted the dynamic topography near the plate boundary and caused rapid rise of the surface topography from west to east (Husson et al., 2014), which further promoted the eastward development of E–W extension. Second, the rollback corresponded with the generally southward migration of the ultrapotassic rocks in the eastern Lhasa terrane relative to the western (Fig. 1b). Subsequently, following the final continental slab breakoff at ∼10–8 Ma, continued eastward flow of lithosphere led to the progressive propagation of kinematically linked conjugate strike-slip faults and north-trending rifts (Fig. 5d).

The integrated working hypothesis proposed here reasonably explains the following observations. First, rifting in the Himalayas developed progressively from west to east. Second, it is compatible between the development of north-trending rifts across the Himalayan-Tibetan system and linked v-shaped conjugate strike-slip faults along the BNS, implying a coupled mechanism between them. Third, most adakitic and ultrapotassic rocks in the Lhasa terrane predate the initiation time of rifting, suggesting that they were not products of the extensional process but independent effects of the geodynamic setting. Fourth, both slab detachment and tearing were manifested by eastward progressive emplacement of post-collisional magmatism. Fifth, the spatiotemporal pattern of post-collisional ultrapotassic magmatism corresponds with a rollback effect for those in the eastern Lhasa terrane relative to the western.

Detailed testable predictions derived from the working hypothesis can be found in the Supplementary Material, and further tests required to validate the working hypothesis are provided here. First, constraints on the activity history of the Woka rift to the north of IYS will strengthen the eastward propagation trend of rifting. The Woka rift is viewed as part of the Woka-Cona rift zone, and thus should follow a similar trend in propagation trend of rifting. Second, accurate geochronological constraints on conjugate strike-slip faults along the BNS are required. This will help to reveal the spatiotemporal pattern of those faults. Third, there should be still-active north-striking normal faults near the edge of eastern or southeastern Tibet due to continued eastward flow of lithosphere.

6. Conclusions

Based on the new thermochronological ages, we conclude that the Cona rift initiated at ∼3.0–2.3 Ma with a horizontal extension magnitude of ∼2–5 km. Late Pliocene initiation of the Cona rift, the sole north-trending rift currently recognized in the eastern Himalaya, highlights it as the youngest rift accommodating E–W extension in the Himalayas. Results from this study and previous research suggest a monotonic eastward development of rifting. We propose an integrated working hypothesis to explain rift propagation and related post-collisional magmatism observed across the Lhasa terrane, which is compatible with key aspects of previous models involving lateral slab detachment, tearing, rollback and lithospheric flow. Eastward lithospheric flow was driven by asynchronous GPE gradients, ultimately modulated by Indian slab dynamics. Eastward-propagating lateral slab detachment led to an associated dynamic topographic rise that built greater GPE in the western Himalaya than the east. This west-to-east progression was enhanced by clockwise toroidal mantle flow around the longitudinally tearing slab. This working hypothesis makes testable predictions for rift initiation and post-collisional magmatic rocks that can be tested by future studies across the Himalayan orogen.

Declaration of competing interest

The authors declare that they have no known competing financial interests or personal relationships that could have appeared to influence the work reported in this paper.

Acknowledgements

Extensive and detailed comments by Dr. Alexander Webb, an anonymous reviewer, and Editor Dr. Rebecca Bendick greatly improved the manuscript. This research is supported by the National Science Foundation of China (Grant Nos. 41472182, 41472181, 41602210, 41330207 and 41720104003), the National S&T Major Project (Grant Nos. 2017ZX05008-001, 2017ZX05003-001), the China Geological Survey (Grant No. 121201102000150009) and the NSF Tectonics Program (EAR 1914501).

Appendix A. Supplementary material

Supplementary material related to this article can be found online at https://doi.org/10.1016/j.epsl.2020.116383.

References

Agius, M.R., Lebedev, S., 2017. Complex, multilayered azimuthal anisotropy beneath Tibet: evidence for co-existing channel flow and pure-shear crustal thickening. Geophys. J. Int. 210, 1823–1844. https://doi.org/10.1093/gji/ggx266.

Armijo, R., Tapponnier, P., Mercier, J.L., Han, T.L., 1986. Quaternary extension in southern Tibet: field observations and tectonic implications. J. Geophys. Res. 91, 13803–13872. https://doi.org/10.1029/JB091iB14p13803.

Bendick, R., Bilham, R., 2001. How perfect is the Himalayan arc? Geology 29, 791–794.

Bendick, R., Flesch, L., 2007. Reconciling lithospheric deformation and lower crustal flow beneath central Tibet. Geology 35, 895–898. https://doi.org/10.1130/G23714A.

Bischoff, S.H., Flesch, L.M., 2018. Normal faulting and viscous buckling in the Tibetan Plateau induced by a weak lower crust. Nat. Commun. 9, 4952. https://doi.org/10.1038/s41467-018-07312-9.

Bureau of Yunnan Geological Survey, 2004. Report of Regional Geological Survey of P. R. China, Longzi County (1:250000). China Geological Survey Special Publication No. H46C004002.

Coleman, M., Hodges, K., 1995. Evidence for Tibetan plateau uplift before 14 Myr ago from a new minimum age for east-west extension. Nature 374, 49–52. https://doi.org/10.1038/374049a0.

Edwards, M.A., Harrison, T.M., 1997. When did the roof collapse? Late Miocene north-south extension in the high Himalaya revealed by Th-Pb monazite dating of the Khula Kangri granite. Geology 25, 543–546. https://doi.org/10.1130/0091-7613(1997)0252.3.CO;2.

England, P., Houseman, G., 1989. Extension during continental convergence, with application to the Tibetan Plateau. J. Geophys. Res., Solid Earth 94, 17561–17579. https://doi.org/10.1029/JB094iB12p17561.

Farley, K.A., Wolf, R.A., Silver, L.T., 1996. The effects of long alpha-stopping distances on (U–Th)/He ages. Geochim. Cosmochim. Acta 60, 4223–4229. https://doi.org/10.1016/S0016-7037(96)00193-7.

Francheteau, J., Jaupart, C., Shen, X.J., Kang, W.H., Lee, D.L., Bai, J.C., Wei, H.P., Deng, H.Y., 1984. High heat flow in southern Tibet. Nature 307, 32–36. https://doi.org/10.1038/307032a0.

Guo, X.Y., Gao, R., Zhao, J.M., Xu, X., Lu, Z.W., Klemperer, S.L., Liu, H.B., 2018. Deep-seated lithospheric geometry in revealing collapse of the Tibetan Plateau. Earth-Sci. Rev. 185, 751–762. https://doi.org/10.1016/j.earscirev.2018.07.013.

Guo, Z.F., Wilson, M., 2019. Late Oligocene-early Miocene transformation of post-collisional magmatism in Tibet. Geology 47, 776–780. https://doi.org/10.1130/G46147.1.

Hou, Z.Q., Zhang, Z.D., Gao, Y.F., Yang, Z.M., Jiang, W., 2006. Tearing and dischronal subduction of the Indian continental slab: evidence from Cenozoic Gangdese volcano-magmatic rocks in South Tibet. Acta Petrol. Sin. 22, 761–774 (in Chinese with English abstract).

Husson, L., Bernet, M., Guillot, S., Huyghe, P., Mugnier, J.L., Replumaz, A., Robert, X., Van der Beek, P., 2014. Dynamic ups and downs of the Himalaya. Geology 42, 839–842. https://doi.org/10.1130/G36049.1.

Kali, E., Leloup, P.H., Arnaud, N., Mahéo, G., Liu, D.Y., Boutonnet, E., Van der Woerd, J., Liu, X.H., Liu, Z.J., Li, H.B., 2010. Exhumation history of the deepest central Himalayan rocks, Ama Drime range: key pressure-temperature-deformation-time constraints on orogenic models. Tectonics 29, TC2014. https://doi.org/10.1029/2009TC002551.

Klootwijk, C.T., Conaghan, P.J., Powell, C.M., 1985. The Himalayan arc: large-scale continental subduction, oroclinal bending and back-arc spreading. Earth Planet. Sci. Lett. 75, 167–183. https://doi.org/10.1016/0012-821X(85)90099-8.

Langille, J.M., Jessup, M.J., Cottle, J.M., Lederer, G., Ahmad, T., 2012. Timing of metamorphism, melting and exhumation of the Leo Pargil dome, northwest India. J. Metamorph. Geol. 30, 769–791. https://doi.org/10.1111/j.1525-1314.2012.00998.x.

Larson, K.P., Kellett, D.A., Cottle, J.M., Camacho, A., Brubacher, A.D., 2020. Mid-Miocene initiation of E–W extension and recoupling of the Himalaya. Terra Nova 32, 151–158. https://doi.org/10.1111/ter.12443.

Lee, J., Hager, C., Wallis, S.R., Stockli, D.F., Whitehouse, M.J., Aoya, M., Wang, Y., 2011. Middle to late Miocene extremely rapid exhumation and thermal reequilibration in the Kung Co rift, southern Tibet. Tectonics 30, TC2007. https://doi.org/10.1029/2010TC002745.

Liang, X.F., Chen, Y., Tian, X.B., Chen, Y.J., Ni, J., Gallegos, A., Klemperer, S.L., Wang, M.L., Xu, T., Sun, C.Q., Si, S.K., Lan, H.Q., Teng, J.W., 2016. 3D imaging of subducting and fragmenting Indian continental lithosphere beneath southern and central Tibet using body-wave finite-frequency tomography. Earth Planet. Sci. Lett. 443, 162–175. https://doi.org/10.1016/j.epsl.2016.03.029.

Lu, T.Y., He, Z.Y., Klemd, R., 2019. Two phases of post-onset collision adakitic magmatism in the southern Lhasa subterrane, Tibet, and their tectonic implications. Geol. Soc. Am. Bull. 21. https://doi.org/10.1130/B35326.1.

Ludwig, K.R., 2003. Isoplot/Ex, A Geochronological Toolkit for Microsoft Excel, Version 3.00. Berkeley Geochronol. Cent., Berkeley.

McCaffrey, R., Nabelek, J., 1998. Role of oblique convergence in the active deformation of the Himalayas and southern Tibet plateau. Geology 26, 691–694. https://doi.org/10.1130/0091-7613(1998)026<0691:ROOCIT>2.3.CO;2.

McDougall, L., Harrison, T.M., 1999. Geochronology and Thermochronology by the ^{40}Ar/^{39}Ar Method, second ed. Oxford University Press, New York.

Meng, J., Gilder, S.A., Li, Y.L., Wang, C.S., Liu, T., 2020. Expanse of Greater India in the late Cretaceous. Earth Planet. Sci. Lett. 542, 116330. https://doi.org/10.1016/j.epsl.2020.116330.

Murphy, M.A., Copeland, P., 2005. Transtensional deformation in the central Himalaya and its role in accommodating growth of the Himalayan orogen. Tectonics 24, TC4012. https://doi.org/10.1029/2004tc001659.

Reiners, P.W., Spell, T.L., Nicolescu, S., Zanetti, K.A., 2004. Zircon (U–Th)/He thermochronometry: He diffusion and comparisons with ^{40}Ar/^{39}Ar dating. Geochim. Cosmochim. Acta 68, 1857–1887. https://doi.org/10.1016/j.gca.2003.10.021.

Seeber, L., Armbruster, J.G., 1984. Some elements of continental subduction along the Himalayan front. Tectonophysics 105, 263–278. https://doi.org/10.1016/0040-1951(84)90207-5.

Tapponnier, P., Xu, Z.Q., Roger, F., Meyer, B., Arnaud, N., Wittlinger, G., Yang, J.S., 2001. Oblique stepwise rise and growth of the Tibet plateau. Science 294, 1671–1677. https://doi.org/10.1126/science.105978.

Taylor, M., Yin, A., Ryerson, F.J., Kapp, P., Ding, L., 2003. Conjugate strike-slip faulting along the Bangong-Nujiang suture zone accommodates coeval east-west extension and north-south shortening in the interior of the Tibetan Plateau. Tectonics 22, 1044. https://doi.org/10.1029/2002TC001361.

Tremblay, M.M., Fox, M., Schmidt, J.L., Tripathy-Lang, A., Wielicki, M.M., Harrison, T.M., Zeitler, P.K., Shuster, D.L., 2015. Erosion in southern Tibet shut down at ∼10 Ma due to enhanced rock uplift within the Himalaya. Proc. Natl. Acad. Sci. 112, 12030–12035. https://doi.org/10.1073/pnas.1515652112.

Turner, S., Arnaud, N., Liu, J., Rogers, N., Hawkesworth, C., Harris, N., Kelley, S., Van Calsteren, P., Deng, W., 1996. Post-collision, shoshonitic volcanism on the Tibetan Plateau: implications for convective thinning of the lithosphere and the source of ocean island basalts. J. Petrol. 37, 45–71. https://doi.org/10.1093/petrology/37.1.45.

Wang, W., Zeng, L.S., Gao, L.E., Wang, Q., Guo, C.L., Hou, K.J., Liu, Z.J., 2018. Eocene-Oligocene potassic high Ba–Sr granitoids in the Southeastern Tibet: petrogenesis and tectonic implications. Lithos 322, 38–51. https://doi.org/10.1016/j.lithos.2018.10.008.

Webb, A.A.D., Guo, H.C., Clift, P.D., Husson, L., Müller, T., Costantino, D., Yin, A., Xu, Z.Q., Cao, H., Wang, Q., 2017. The Himalaya in 3D: slab dynamics controlled mountain building and monsoon intensification. Lithosphere 9, 637–651. https://doi.org/10.1130/L636.1.

Webb, A.A.G., Yin, A., Dubey, C.S., 2013. U-Pb zircon geochronology of major lithologic units in the eastern Himalaya: implications for the origin and assembly of Himalayan rocks. Geol. Soc. Am. Bull. 125, 499–522. https://doi.org/10.1130/B30626.1.

Wortel, M.J.R., Spakman, W., 2000. Subduction and slab detachment in the Mediterranean-Carpathian region. Science 290, 1910–1917. https://doi.org/10.1126/science.290.5498.1910.

Xu, B., Griffin, W.L., Xiong, Q., Hou, Z.Q., O'Reilly, S.Y., Guo, Z., Pearson, N.J., Gréau, Y., Yang, Z.M., Zheng, Y.C., 2017. Ultrapotassic rocks and xenoliths from south Tibet: contrasting styles of interaction between lithospheric mantle and asthenosphere during continental collision. Geology 45, 51–54. https://doi.org/10.1130/G38466.1.

Xu, Z.Q., Wang, Q., Pêcher, A., Liang, F.H., Qi, X.X., Cai, Z.H., Li, H.Q., Zeng, L.S., Cao, H., 2013. Orogen-parallel ductile extension and extrusion of the Greater Himalaya in the late Oligocene and Miocene. Tectonics 32, 191–215. https://doi.org/10.1002/tect.20021.

Yang, Y.J., Ritzwoller, M.H., Zheng, Y., Shen, W.S., Levshin, A.L., Xie, Z.J., 2012. A synoptic view of the distribution and connectivity of the mid-crustal low velocity zone beneath Tibet. J. Geophys. Res., Solid Earth 117, B04303. https://doi.org/10.1029/2011JB008810.

Yang, Y.Q., Liu, M., 2013. The Indo-Asian continental collision: a 3-D viscous model. Tectonophysics 606, 198–211. https://doi.org/10.1016/j.tecto.2013.06.032.

Yin, A., 2010. Cenozoic tectonic evolution of Asia: a preliminary synthesis. Tectonophysics 488, 293–325. https://doi.org/10.1016/j.tecto.2009.06.002.

Yin, A., Dubey, C.S., Kelty, T.K., Webb, A.A.G., Harrison, T.M., Chou, C.Y., Célérier, J., 2010. Geologic correlation of the Himalayan orogen and Indian craton: Part 2. Structural geology, geochronology, and tectonic evolution of the eastern Himalaya. Geol. Soc. Am. Bull. 122, 360–395. https://doi.org/10.1130/B26461.1.

Yin, A., Harrison, T.M., 2000. Geologic evolution of the Himalayan-Tibetan orogen. Annu. Rev. Earth Planet. Sci. 28, 211–280. https://doi.org/10.1146/annurev.earth.28.1.211.

Yin, A., Taylor, M.H., 2011. Mechanics of V-shaped conjugate strike-slip faults and the corresponding continuum mode of continental deformation. Geol. Soc. Am. Bull. 123, 1798–1821. https://doi.org/10.1130/b30159.1.

Zandt, G., Humphreys, E., 2008. Toroidal mantle flow through the western U.S. slab window. Geology 36, 295–298. https://doi.org/10.1130/G24611A.1.

Zhang, L.Y., Ducea, M.N., Ding, L., Pullen, A., Kapp, P., Hoffman, D., 2014. Southern Tibetan Oligocene-Miocene adakites: a record of Indian slab tearing. Lithos 210–211, 209–223. https://doi.org/10.1016/j.lithos.2014.09.029.

Zhang, Z.J., Chen, Y., Yuan, X.H., Tian, X.B., Klemperer, S.L., Xu, T., Bai, Z.M., Zhang, H.S., Wu, J., Teng, J.W., 2013. Normal faulting from simple shear rifting in Southern Tibet, using evidence from passive seismic profiling across the Yadong-Gulu Rift. Tectonophysics 606, 178–186. https://doi.org/10.1016/j.tecto.2013.03.019.

Zheng, G., Wang, H., Wright, T.J., Lou, Y.D., Zhang, R., Zhang, W.X., Shi, C., Huang, J.F., Wei, N., 2017. Crustal deformation in the India-Eurasia collision zone from 25 years of GPS measurements. J. Geophys. Res., Solid Earth 122, 9290–9312. https://doi.org/10.1002/2017JB014465.

Zuza, A.V., Wu, C., Reith, R.C., Yin, A., Li, J.H., Zhang, J.Y., Zhang, Y.X., Wu, L., Liu, W.C., 2018. Tectonic evolution of the Qilian Shan: an early Paleozoic orogen reactivated in the Cenozoic. Geol. Soc. Am. Bull. 130, 881–925. https://doi.org/10.1130/B31721.1.